Corrosion behavior and microstructural characterization of friction stir welded API X70 steel

J. M. Giarola[1], J. W. Calderón-Hernández[2], F. F. Conde[1], J. B. Marcomini[1], H. G. de Melo[2]
*J.A. Avila[3], W. W. Bose Filho[1]

1. USP – University of São Paulo, Av. Trabalhador São Carlense 400, São Carlos, SP, 13566590, Brazil.
2. Departamento de Eng. Metalúrgica e de Materiais, EPUSP, Av. Prof. Luciano Gualberto, 380 - Butantã, São Paulo - SP, 05508-010, Brazil
3. UNESP – São Paulo State University (UNESP), Campus of São João da Boa Vista, São João da Boa Vista, SP, Brazil.

***Corresponding author**: Julian Avila, julian.avila@unesp.br

Abstract

Friction stir welding is an excellent alternative process used in pipelines circumferential welds due to fusion welding low corrosion resistance. This study describes the corrosion resistance as a function of the microstructural features resulting from an API X70 FSW weld joint. The microstructural features were examined by optical microscopy, scanning electron microscopy, and X-ray diffraction. The corrosion analysis was conducted employing potentiodynamic polarization tests using an electrochemical microcell, which allowed to test small circular areas delimited by a 2mm in diameter O-ring gasket. The base metal and heat-affected zone were the most susceptible region to corrosion due to the banded microstructures, and the re-stirred-zone and stir zone was the most resistant region to corrosion because of grain refinement.

Keywords: friction stir welding; corrosion resistance; corrosion rate; potentiodynamic polarization tests; electrochemical microcell

1. Introduction

A vast amount of energy is used across the planet and most of it is supplied by fossil fuels, such as petroleum and natural gas, increasing its demand and leading to the exploitation of new oil wells in deep waters and hostile environments [1,2]. A significant part of the pipelines used for the transport of such resources is made of steel. They transport the fluids over extensive distances and are, in many cases, exposed to hostile environments and for long periods. As mechanical strength and fracture toughness are paramount requirements, these

pipelines are made of microalloyed low-carbon steels, thus delivering transport efficiency under severe environmental conditions [2,3].

However, steels and other metallic alloys may be susceptible to stress corrosion cracking (SCC) and hydrogen-induced cracking (HIC) [2]. From experience, it has been observed that localized corrosion in welds is the most common mode of in-service failures of pipelines made from steel [4], which may lead to irreversible environmental damage. It was suggested by some authors [5–8] that welding pipeline steel should enhance corrosion susceptibility due to metallurgical changes and reduced tensile residual stresses. The microstructural differences between the weld zone and the base steel could result in an electrochemical galvanic effect, enhancing corrosion susceptibility [7].

Friction stir welding (FSW) is a solid-state joining process, resulting in microstructural and metallurgical features with different corrosion behavior than that from fusion welding joints. Remarkably, no filling metal is necessary, and the fusion of the metal is not involved. As lower peak temperatures are employed during the FSW process, the resulting residual stresses should also be lowered [9]. Besides, the transition between the heat-affected zone (HAZ) and the stir zone (SZ) must constitute a less harmful zone than that present in the arc welding process, not exhibiting significant grain coarsening and brittleness [10]. These and other characteristics may affect FSW corrosion behavior, and as far as our knowledge, they have not been well studied for High Strength Low Alloy (HSLA) steels used for tubing in oil and gas industries.

In arc welding, several studies [4,8,11–14] showed that due to high-temperature peak, the material microstructure changes, generating microstructural gradient zones of different properties, according to the distance from the fused bead. Usually, the HAZ presents the lowest corrosion resistance, limiting the components' application [4,8,11–14]. Zhang and Cheng [7] studied the welded X70 pipeline steel's local dissolution mechanism in a near-neutral pH solution (NS4 solution). The results showed similar corrosion resistance through all zones, except for HAZ, showing a maximum current and anodic dissolution activity.

FSP and FSW present similar microstructures and mechanical properties, as reported in previous studies for one-pass bead-on- plate [15] and welded joint [16]. The corrosion resistance assessed of interstitial free steel welded by FSP was investigated by Wang et al. [17]. The corrosion potential (Ecorr) and corrosion current density (icorr) were obtained from the 3.5% NaCl solution's polarization curves. They reported an Ecorr and icorr of the friction stir processing (FSP) specimen more positive and lower than those of the base metal (BM), indicating that the FSP exhibited lower corrosion rates compared with the BM. Regarding the fatigue cycle behavior, FSP samples presented better performance than BM samples in both air and NaCl solution, which were lower in the latter solution. In other studies conducted with

low carbon steel FSW joint, the specimens' corrosion behavior from the welded region and base metal was determined by potentiodynamic polarization method in a 3.5 % NaCl solution [18]. The BM current density decreased from 4.44 μA/cm^2 to 3.36 μA/cm^2 after FSW, while the corrosion rate value decreased from 1.75 to 1.32 mpy (mils (0,001 in) per year) after FSW. Thus, the literature shows that corrosion resistance increases after the FSW process.

Most of the corrosion studies of welded low carbon steels involve conventional welding processes based on the fusion of the material and how the microstructural and metallurgy features are related to the final corrosion behavior. Therefore, the literature on how the FSW process affects low carbon steel corrosion properties is scarce, especially in pipelines. This article aims to describe the corrosion behavior and the FS-Welded joint's microstructural features conducted in API X70 steel plates. The corrosion resistance was assessed using potentiodynamic polarization tests at different welding regions, i.e., heat affected zone (HAZ), stir zone (SZ), hard zone (HZ), re-stirred zone (RSZ), and base metal (BM). To investigate the corrosion behavior in these zones, an electrochemical microcell (2mm diameter, 3.14mm^2) was used to conduct the experiments. Microstructural changes were examined by optical and scanning electron microscopes (SEM), X-ray diffraction (XRD), and basic mechanical properties evaluated based on Vickers hardness measurements.

2. Experimental procedure

2.1 Material

The API 5L X70 steel 18 mm thickness plates were fabricated using a thermomechanical control process. The chemical composition was determined by optical emission spectrometer ANACOM brad B2 Advanced and is shown in Table 1.

Table 1. Chemical composition of the API 5L X70 steel in wt. %.

C	Si	Mn	P	S	Cr	Ni	Mo	Nb	V	Ti
0.009	0.19	1.59	0.010	0.003	0.02	0.21	0.04	0.055	0.046	0.011

2.2. Welding parameters

The FSW joints were oriented parallel to the API 5 plate rolling direction. A two-pass bead-on-plate configuration was used to weld by FSW. The FSW tool was composed of a

metallic matrix composite PCBN–WRe, 25%Re–W alloy reinforced with 60%vol PCBN (Polycrystalline Cubic Boron Nitride). Such a tool presented a 9.5 mm long threaded conical pin and a convex threaded shoulder. The weld's penetration depth was approximately equal to the pin length, which necessitated a two-pass welding procedure where a weld was repeated on both sides of the plate. The FSW was carried out under a force control mode with 100 mm min^{-1} travel speed, 300 RPM spindle speed, and a 39 kN axial force. Figure 1 shows the FSW setup and coordinates schematically. These processing conditions have presented the best results in previous studies [15,16,19,20]

The welding process is not symmetrical concerning the line or plane that defines it due to the rotation movement and the material flow around the tool. In this way, the feed advancing side (AS) is defined, with the highest relative speed of the tool, in which the direction of rotation of the tool is the same as that of the welding, producing plastic deformation and more severe thermal exposure, and the withdrawal retreating side (RS) at which the tool rotation is opposite to its travel direction [21,22].

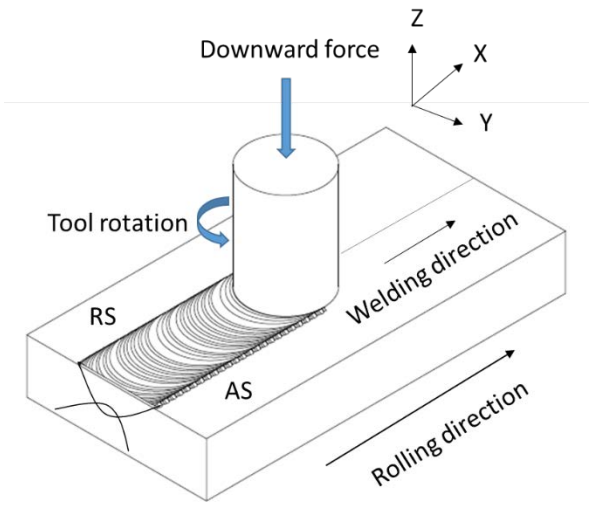

Figure 1. Schematic representation of the FSW process.

2.3. Microstructural characterization

For the welded joint metallographic characterization, scanning electron microscopy (SEM) and light optical microscopy (LOM) were used. The nonmetallic inclusions were analyzed according to ASTM E 45 standard [23].

Metallography samples were ground and polished following the ASTM E3-17 [24], and Nital 2 % etchant was used to reveal the grain boundaries. A computer-controlled microdurometer was used for the hardness line-scanning of the welded joints. The Vickers indentation was carried out according to ASTM E 384-17 standard [25], on the micro-scale,

with 200 g and 15 s load and dwell time, respectively. The microhardness profiles were obtained in the middle of the 1st and 2nd passes. Grain size analysis and secondary phases quantification were analyzed from images obtained with SEM and using the Image J software. The secondary phases (SP) were quantified in the area image, which was extrapolated to volume percentage. Notice that SP and constituents are divided into martensite-austenite (MA), degenerated pearlite (DP), bainite (B), and martensite (M), and their presence depends on the cooling rate [26,27].

For X-ray diffraction (XRD) analysis, a Bruker XRD 8 Advance diffractometer was used, with 1000 W power and a Cu Kα radiation. The wave energy was 8.04 keV, and the wavelength of 1.5406 Å. The sample was scanned from 5 to 90°, step size of 0.02°, and an acquisition time of 2 seconds for each position. A diffraction pattern was retrieved from the diffraction data to enable a qualitative and quantitative analysis of the API 5L X70 steel phase composition. The austenitic phase was quantified, applying Eqs. 1 and 2 from [28]. These equations consider the diffracted peaks area, the structure and multiplicity factors for each peak, and each phase-type effects on the measured volume. In which, F_p is the phase fraction of phase p, n_p is the number of peaks from phase p, K represents a given {*hkl*} family, I_{pK} is the area below a peak for family K on phase p and RpK is a dimensionless scalar containing the effects of the remaining parameters, R_{pK} correlates the volume of the unit cell of phase p (V), the phase structure factor (f) and multiplicity factors (M_K) for each family of planes.

$$F_p = \frac{\frac{1}{n_p}\sum_K^{n_pK}\frac{I_{pK}}{R_{pK}}}{\sum_p\frac{1}{n_p}\sum_K^{n_pK}\frac{I_{pK}}{R_{pK}}} \quad (1)$$

$$R_{pK} = \frac{f_K^2 x M_K}{V_p^2} \quad (2)$$

2.4. Corrosion behavior

The electrochemical measurements were performed in a 3.5 % NaCl solution in samples machined from the X70 steel welded plates cross-section. The sample was ground up to 600-grit emery paper and cleaned using alcohol and deionized water. A standard three-electrode cell was used, i.e., the BM and the different FSW regions of the X70 pipeline steel as a working electrode, a silver/silver chloride (Ag/AgCl, KCl saturated) as the reference electrode, and a platinum wire as the counter electrode. Figure 2 shows the electrochemical microcell used to carry out the electrochemical tests at each different welded joint region. A

circular area of 2mm diameter was delimited using an O-ring gasket. Therefore, the corrosion resistance of the BM, HAZ, SZ, HZ, and RSZ was assessed separately.

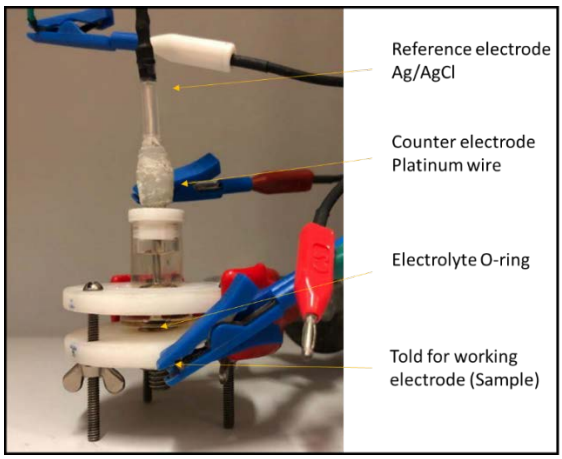

Figure 2. Electrochemical microcell arrangement.

After immersion in the test electrolyte, the working electrode remained for 30 min at the open circuit potential (OCP) to reach a stable value. The potentiodynamic polarization tests were carried out from -100 mV from the OCP until the anodic current density reached 1 mA/cm^2. A scan rate of 1 mV/s was applied. Three measurements were done in every specific zone to guarantee reproducibility

The 3.5% NaCl is an overly aggressive electrolyte, which possibly caused Ecorr values to be similar, with values around -0.700 V. A less aggressive solution could differentiate the regions better. Nevertheless, 3.5% NaCl was chosen since it representing the aggressive of real service environments like seawater. Additionally, it is an electrolyte entirely used in literature, which compares with corrosion values reported with another welding process, such as submerged arc welding (SAW) and FSW[18,29].

From the corrosion current density (icorr) determined using the Tafel extrapolation methodology, the corrosion rates (mpy) were calculated from Faraday´s law by using Eq 3 [30]. M is the atomic mass (g/mol), m is the oxidation state or valence, ρ is density (g/cm^3), icorr (mA/cm^2).

$$CRP\ (mpy) = 0{,}0129\frac{M\ icorr}{m\rho} \qquad (3)$$

3. Results

3.1. Microstructural Characterization

The microstructural characterization was performed in three areas: BM, SZ, and HAZ. The SZ can be further subdivided into three regions: conventional SZ, hard zone (HZ), and re-stirred zone (RSZ), as depicted in Figure 3, and the HAZ can be further subdivided into two regions: high temperature (HT-HAZ) and low temperature (LT-HAZ) regions. The LT-HAZ did not undergo microstructural changes concerning the MB. This Figure also shows the equivalent grain size and few secondary phases (SP), which are addressed to carbides, degenerated pearlite, M/A, and cementite debris [27]. The equivalent grain size was determined based on the number of grains visible and crossed by a line. This analysis disregards the large size of the bainite packets and considers the plates within these bainites.

The BM's microstructure comprises elongated and packed ferrite grains due to the rolling process, some equiaxed and polygonal ferritic grains, and SP bands, as shown in Figure 3b. The HAZ, depicted in Figure 3c, presents a coarse-grained microstructure formed by bainite packets B(P) and granular bainite (GB).

The SZ's microstructure, depicted in Figure 3d, is mainly composed of GB and some B(P). The HZ, Figure 3e, displays lath type structure formation, bainite packets with irregular and straight plates B(P). The RSZ is formed due to FSW's overlap; hence, it is twice stirred and undergoes a re-heating, thus changing the first pass's microstructure. This heat flux caused austenitization and recrystallization, resulting in a microstructure predominantly of polygonal ferrite and secondary phases, shown in Figure 3e. The analyses reveal refinement of all FSW microstructure in comparison to BM.

Except in the SZ (Figure 3(d)), the proportion of SP in most regions is the same, yet in the FSW regions, they are more finely dispersed than in the BM. Due to the high cooling rates after FSW, the SP tends to be finer than under slow cooling rates. Rapid cooling rates favor bainitic products, and slow cooling rates the formation of polygonal and quasi-polygonal products [26].

Figure 4 shows the XRD spectra of the SZ and BM, respectively, with the peak positions for ferrite and austenite. The volume fraction of retained austenite is low when compared to ferrite. Retained austenite quantified in the BM and welding region was less than 2%.

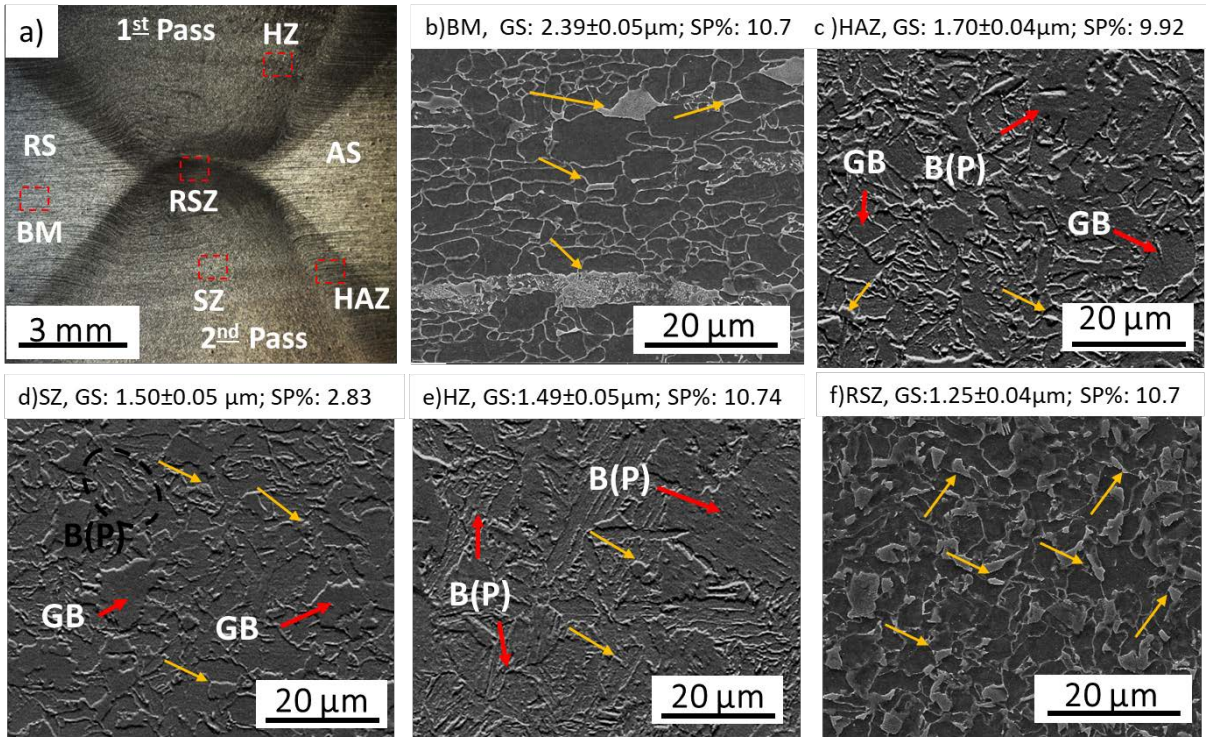

Figure 3. Optical (a) and scanning electron micrographs (b, c, d, e, f) for microstructural characterization of the FSW API X70 steel. a) macrography showing double FSW pass and overlap at the center-root of the joint; b) BM; c) HAZ; d) SZ; e) HZ; f) RSZ. GB: Granular bainite, B(P): Bainite with irregular and straight plates. The yellow arrow depicts the position of some secondary phases. GS stands for equivalent grain size and SP for the presence of the secondary phase.

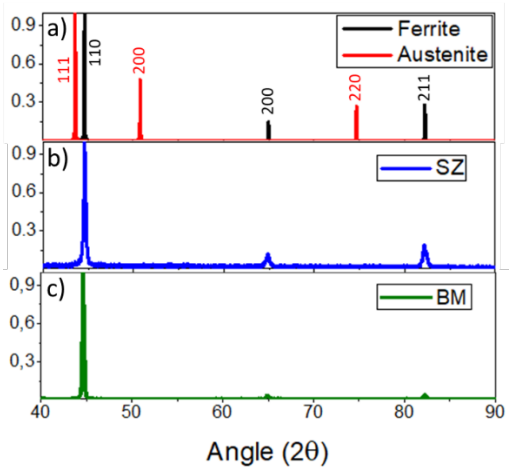

Figure 4. a) Theoretical peaks positions of ferrite and austenite diffraction patterns. X-ray diffraction spectra of the API X70 steel: b) SZ, and c) BM.

The inclusions analysis assessed the purity of the studied steel and was performed according to ASTM E 45 standard [23]. The outcomes, shown in Table 2, revealed a significant inclusions content and indicated that the FSW process did not affect their size distribution. Findings showed a predominance of inclusions of D type in both conditions. Most oxides present a globular morphology. The other regions of the welded joint showed similar behavior to SZ.

Table 2. Nonmetallic inclusions analysis, according to ASTM E 45.

	THIN SERIES				THICK SERIES			
	A	B	C	D	A	B	C	D
BM	2	2	0	2.5	0.5	0.5	0	1
SZ	1.5	2	0	3	1	1	0	1.5

3.2. Hardness

Figure 5 depicts the two-passes joint's hardness profile in the 1st and 2nd FSW pass, presenting similar values between passes, suggesting a homogeneous welding procedure. The BM region presented the lowest mean hardness value than the areas formed due to the FSW process. HAZ showed an increase of hardness due to the complete austenitization and rapid cooling, contributing to form acicular microstructures such as bainite packets [20,21,26].

Significant changes occurred in the SZ microstructure, resulting in a region with the highest hardness among the formed microstructures. During the FSW, the SZ is subjected to asymmetric heat input, causing differences between sides and material mechanical flow. The advancing side (AS in Figure 1) generates higher heating input than the retreating side due to the higher friction and force necessary to move the material at the front of the spinning tool [21]. The retreating side (RS in Figure 1) has the mechanical flow facilitated due to a contrary movement between tool rotation and advance. While the tool advances, the spinning tool drags material backward, easing the deformation process.

Consequently, the hard-zone (HZ) is usually located at the advancing side [21]. [16,21,31], at which the high hardness can be ascribed to bainite formation in plates. The first pass HZ hardness (310.5± 40.6HV) is lower than the HZ hardness in the second pass (353.1± 26.9). This microstructural feature can be attributed to the second pass tempering effect on the first pass [32].

A hardness decrease inside the RSZ was observed in comparison to the SZ. The hardness measured at the interface between the two passes indicated no difference in contrast to the BM hardness, with a mean value of 207.7± 6.2HV.

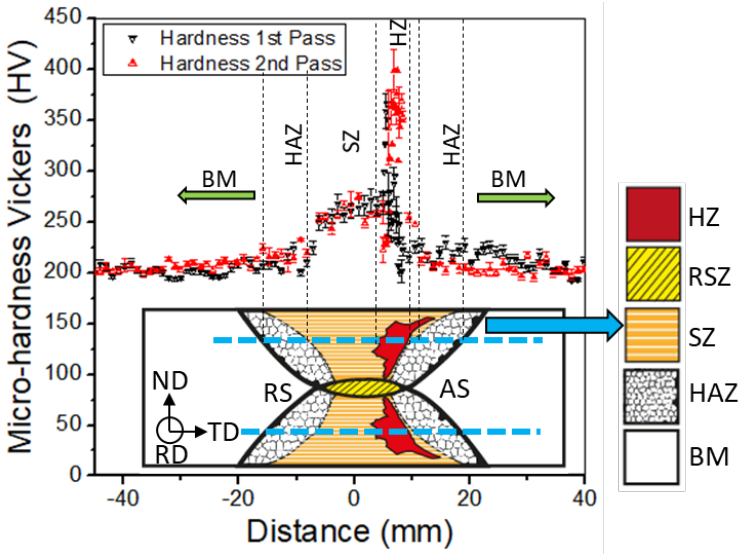

Figure 5. Vickers hardness profile of the welded joint at the 1st and 2nd passes.

3.5. Corrosion resistance

Figure 6 shows representative potentiodynamic polarization curves acquired at each specific zone of the welded joint. The anodic and cathodic branches show activation-controlled processes and similar shapes for all the investigated conditions, indicating similar corrosion mechanisms. The curves also show that, for all weld zones, both the cathodic and the anodic branches are more polarized than the BM, indicating a slower dissolution process. On the other hand, all the curves practically overlap among the weld zones, except for the anodic branch of the RSZ, which was slightly more polarized.

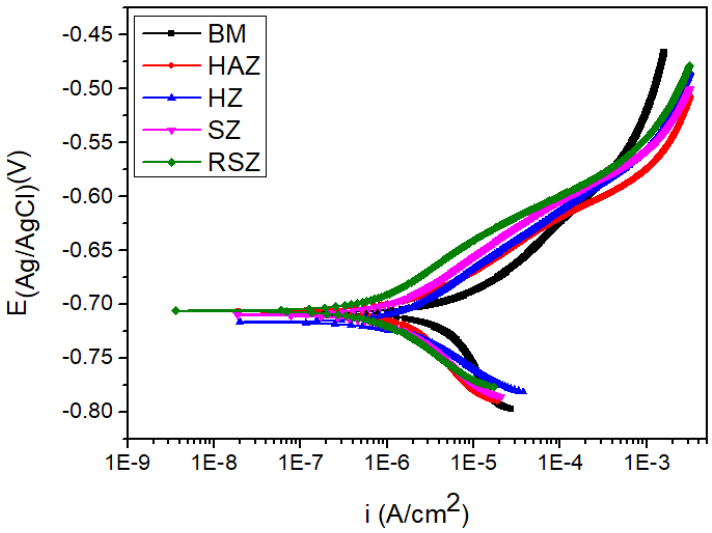

Figure 6. Representative potentiodynamic polarization curves were obtained in a 3.5% NaCl solution for the BM and the different FSW regions of X70 steel.

The corrosion potential (Ecorr) values were obtained directly from the plots (when the current sign changed), whereas the corrosion current density (icorr) for each weld zone and the BM was determined by Tafel extrapolation of both the anodic and the cathodic branches of the polarization curves. The outcomes are summarized in Figure 7. Each determination displays an error bar to take into account the results of all representative experiments. No significant difference could be detected between the Ecorr values (Fig. 7(a)). On the other hand, Figure 7(b) indicates that the weld zone's corrosion resistance is improved compared with the BM, except for the HAZ, which icorr was in the same order of magnitude. The results displayed in Figure 7(b) allow to rank the corrosion resistance as follows: RSZ ≅ SZ > HZ > HAZ ≅ BM. The weld region's microstructural refinement and homogenization may account for this improvement in the corrosion resistance compared to the BM. The microstructural gradient of the HZ and HAZ, caused by differences in the fraction of bainite, could account for the high standard deviation in these particular regions compared to the others.

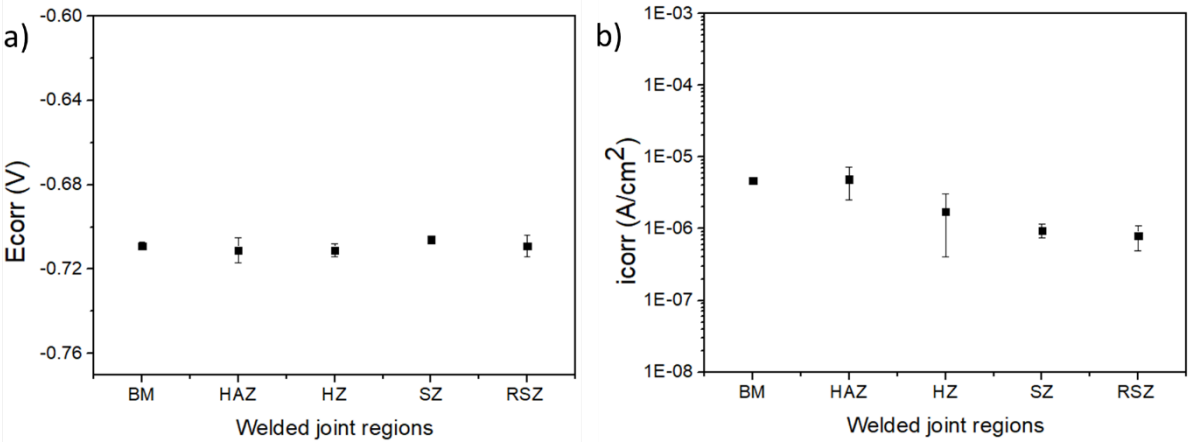

Figure 7. Electrochemical parameters of the different weld regions and base metal: a) Ecorr b) icorr.

4. Discussion

The microstructural transformations leading to a lath-type structure, B(P) in the HZ region, may be responsible for almost 100HV hardness increase compared to 206HV of the BM. Baker et al. reported individual fine particle precipitation on lath boundaries and even thin film precipitation morphology [33]. This fact indicated the possible correlation with the hardness increase of some FSW zones observed by these authors [33] and may well correlate with the increased hardness of the HZ verified in the present work. The RSZ was formed by the overlap of the 2nd pass over the 1st pass, resulting in a similar hardness to the BM. The microstructure

in this region was mainly composed of polygonal ferrite, and the diffusional process favored secondary phases (SP) with the same ratio aspect as in the matrix grains.

There is a consensus in the literature for steels containing relatively high inclusions levels that these microstructural features play a central role in the corrosion behavior [11,34–36]. In general, the inclusions' electrochemical behavior differs from the matrix, forming galvanic microcells, serving as initiation sites for localized corrosion [36]. An outcome that is at variance with the documented in the work of Zhang et al. (2016) for a high nitrogen stainless steel joined by FSW. They reported that inclusions in the BM were re-dissolved and refined because of the thermal cycle and strong stirring effect during FSW, which has a beneficial impact on the improvement of corrosion resistance in 3.5 wt.% NaCl [12].

The thicknesses losses (mpy) for each weld region, and the BM were calculated employing Eq 3 using the mean icorr values displayed in Figure 7. The results, plotted in Figure 8 along with the equivalent grain size and SP volume fraction, indicating that the yearly-based thickness reduction in mils (0.001 in) is higher at the BM and HAZ, corresponding to the zones more susceptible to corrosion. On the other hand, the lowest corrosion rate was determined at the SZ and RSZ. This Figure also demonstrates that, except for the HAZ (addressed later), the smaller the grain size, the lower the corrosion rate.

Microstructural changes in the weld zone can explain the slight increase in its corrosion resistance after FSW. Many authors [14,37,38] denote that refined grains compared to coarse grains decrease corrosion rates. Moreover, as reported in the literature [38], grains refinement may cause homogenization of the microstructure, uniform distribution of phases, and reduced lattice defects, thus decreasing the differences between local anodic and cathodic sites.

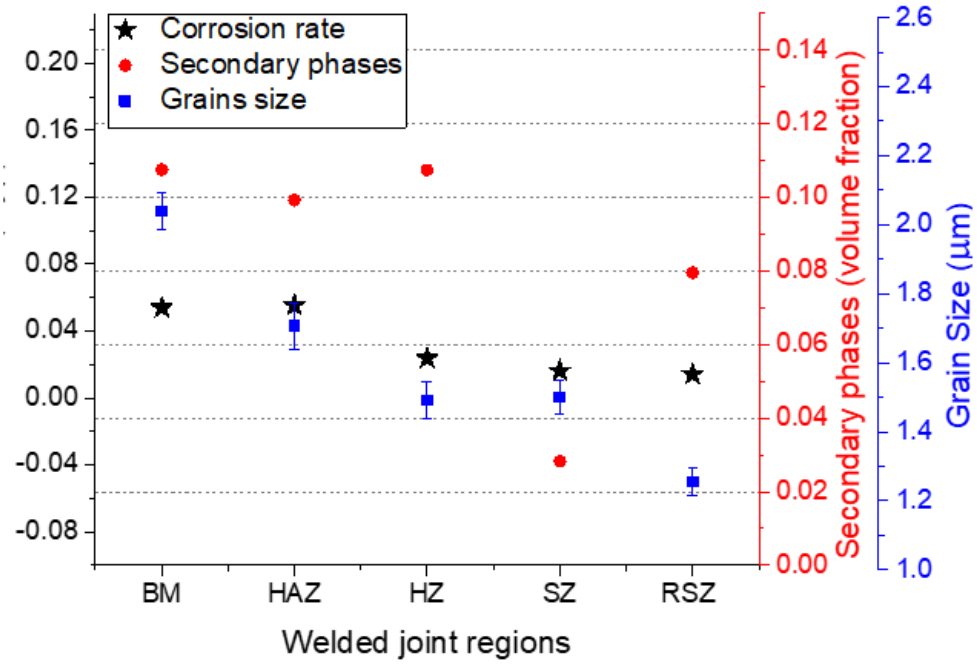

Figure 8. Comparison between the corrosion rate, the volume fraction of secondary phases, and grain sizes for the BM and the different weld zones.

Galvanic coupling between ferrite and cementite enhances ferrite corrosion [39]. As in the BM, ferrite and pearlite are separated in a banded structure. This distribution may increase the former phase's corrosion due to the effect of cementite present in the latter [40]. Thus, the homogenization in the FSW regions can reduce galvanic corrosion [41]. Moreover, although cementite and ferrite's galvanic effects could still feed corrosion within bainite grains [39], the grain refinement detected in the FSW process causes a local reduction in the cathodic-anodic ratio in the welded regions, improving their corrosion resistance [18,41]. Grain refinement affords many local corrosion initiation sites, as the areal density of grain boundaries increases, causing the individual pits to form relatively small and shallow. Thus, the increase in the number of local corrosion sites in the fine-grained microstructure leads to a decrease in the corrosion process as the phenomenon's driving force is weakened [18,42].

Another factor that could also improve the weld zones' corrosion resistance in FSW is the partial solubilization of carbides [41]. Carbon may be partially solubilized in retained austenite, forming a M/A constituent, instead of precipitate as carbides [41]. Together with homogenization (as discussed above), this mechanism may also contribute to local reduction in galvanic corrosion between ferrite and cementite, thus improving the overall corrosion resistance in the SZ [39]. Cruz et al. [41] found a similar behavior, in which the progressive homogenization of the microstructure in the SZ due to partial solubilization of carbides

increased the charger transfer resistance at the interface, thus improving the corrosion resistance.

The HAZ behavior differed from the other weld regions, showing a corrosion rate similar to the BM; Avila et al. [20] reported that FSW joints present a complex HAZ. The authors claim [20] that part of the HAZ does not present microstructural changes compared to the BM, which was denominated as low temperature HAZ (LT-HAZ). Although this region was not reported in Figure 3, as it is not the main focus of this work, it was also identified in the microstructure. The LT-HAZ corresponds to a large part of the HAZ and, similar to the BM, shows banded microstructure; thus, this factor may have been responsible for the similarities in these two regions' corrosion rates.

Although the studied microstructures share a ferrite nature, as shown in Figure 4, it was possible to detect differences in the weld regions' corrosion behavior utilizing the microcell, which was mainly ascribed to grain refinement microstructure and homogenization. Therefore, a slight overall increase in the weld zones' corrosion resistance was verified compared with the BM, which is technologically essential. The results obtained in the present work are corroborated when comparing the results obtained by FSW with conventional welding processes published in the literature. Table 3 contrasts the corrosion rates collected with the FSW process and other welding types to exemplify this phenomenon. Even though significant data scattering can be verified, which can be ascribed to the different experimental conditions, as verified in the present work, the results report a decrease in the weld zone's corrosion rate when the joining procedure was the FSW. For the other joining procedures, the weld zone becomes more susceptible to corrosion.

Notice a significant change between results from different authors. The results showed for Cruz et al. [41] justified the divergence due to the authors' acid medium was pH 4, which caused corrosion products. The corrosion products were better distributed within SZ and HZ than those in the BM, HAZ, and TMAZ, promoting a better protective effect on the welded regions' surface. In the same medium, 3.5 % NaCl, Sekban et al. [14] reported similar corrosion rates to this work. However, with conventional welding, the corrosion rates were high. The API X52 steel, with submerged arc welding (SAW) processing, found corrosion rates fifty times higher in the region welding than SZ for FSW, demonstrating that FSW is an alternative technology for pipeline joints.

Table 3: Compared FSW with conventional welding corrosion rates.

Authors	**Electrolyte**	**Steels** **C: %wt**	**Weld process**	**Base Metal** **Ecorr (mV)** **CR (mpy)**	**Weld Zone** **Ecorr mV)** **CR (mpy)**
Current Investigation	3.5% NaCl	API X70 C: 0.009%	FSW	-707 **2.15**	-705 **0.37 (SZ)**

					-709 **2.25 (HAZ)**
D.M. Sekban el at (2019) [18]	3.5% NaCl	Low-carbon shipbuilding plates - C: 0.16%	FSW	-665 **1.17**	-708 **1.32**
J.R. da Cruz (2020) [41]	Na2SO4 pH:4 (De-aerated)	API X70 C: 0.17	FSW	-506 **21.50**	-476 **18.76**
K.M. Deen (2010) [43]	0.5% NaCl	ASTM 516 G70 C: 0.18%	SAW	-779 **3.2**	-719 **5.9**
H. Tristijanto et al. (2020) [29]	3.5% NaCl	API X52 C:0.065%	SAW	-590 **14.2**	-634 **53.5**
W. Liu et al. (2017) [44]	3.5% NaCl	HSLA C:0.09%	VEGW SAW	-471 **7.69** -472 **7.82**	-530 **9.79** -547 **10.55**

4. Conclusions

A BM consisting of a matrix of equiaxial ferritic grains and second phases bands evolved to bainite with the granular bainite (GB) and bainite packets B(P) morphology in the HAZ and SZ. The proportion of B(P) with straight plates is higher in the HZ than the rest of the SZ. Simultaneously, the RSZ presented a refined microstructure, with a similar aspect ratio of second phases resulted in a softening compared to the rest of the SZ.

Base metal composed of banded microstructures of ferrite and perlite and HAZ partially composed for the same microstructure presented more corrosion taxes than other friction stir weld zones. The higher charge transfer resistance of weld zones was caused by grains´ refining, which led to homogenization in those regions that reduced the galvanic corrosion. The corrosion potential (Ecorr) was not affected by the microstructures' differences within the FSW welded joints. In this specific environment, the solution was aggressive and did not allow differentiating between the regions

The steel analyzed exhibited a high level of inclusions, and it is possible to infer that there was a problem in the manufacture of liquid steel. The inclusions suffered a redistribution due to the FSW process and did not affect its corrosion behavior.

Acknowledgments

Joseane Giarola would like to acknowledge the National Council for Scientific and Technological Development, CNPq", Scholarship - Brazil." Process: 165065/2017-6. The author recognizes the use of the SMM, EESC-USP facilities, and Dr. Julián Escobar for treated the X-ray diffraction data. Research supported by LNNano - Brazilian Nanotechnology National

Laboratory, CNPEM/MCTIC. Thanks to MIB, Instituto de Materiais Tecnológicos do Brasil Ltda., for the operation of the chemical composition experiment.

Ethical Approval

This research did not involve Human Participants or Animals; thus, ethical approval is not necessary.

Consent to Participate:

This research did not involve Human Participants; thus, a consent of participation is not necessary.

Consent to Publish:

This research did not involve Human Participants; thus, Consent to Publish is not necessary.

Authors Contributions:

- J. M. Giarola: Data curation; Formal analysis; Writing – original draft
- J. W. Calderón-Hernández: Investigation; Writing - review & editing.
- F. F. Conde: Investigation
- J. B. Marcomini: Investigation
- H. G. de Melo: Investigation; Writing - review & editing.
- J.A. Avila: Conceptualization; Supervision; Data curation; Formal analysis; Writing
- W. W. Bose Filho: Conceptualization; Supervision; Data curation; Formal analysis; Project administration; Writing

Funding:

Joseane Giarola would like to acknowledge the National Council for Scientific and Technological Development, CNPq", Scholarship - Brazil." Process: 165065/2017-6

Competing Interests:

The authors reported no potential conflict of interest.

Availability of data and materials:

The data that support the findings of this study are available from the corresponding author, [J.A. Avila], upon reasonable request.

Disclosure statement:

The authors reported no potential conflict of interest.

References

[1] Canada's Oil e Natural Gas producers, Who Uses the Most Energy ?, (2020). https://www.capp.ca/energy/world-energy-needs/ (accessed May 28, 2020).

[2] M.A. Mohtadi-Bonab, J.A. Szpunar, R. Basu, M. Eskandari, The mechanism of failure by hydrogen induced cracking in an acidic environment for API 5L X70 pipeline steel, Int. J. Hydrogen Energy. 40 (2015) 1096–1107. https://doi.org/10.1016/j.ijhydene.2014.11.057.

[3] A. Thomas, J.A. Szpunar, Hydrogen diffusion and trapping in X70 pipeline steel, Int. J. Hydrogen Energy. 45 (2019) 2390–2404. https://doi.org/10.1016/j.ijhydene.2019.11.096.

[4] L.W. Wang, Z.Y. Liu, Z.Y. Cui, C.W. Du, X.H. Wang, X.G. Li, In situ corrosion characterization of simulated weld heat affected zone on api x80 pipeline steel, Corros. Sci. 85 (2014) 401–410. https://doi.org/10.1016/j.corsci.2014.04.053.

[5] K.-M. Moon, M.-H. Lee, K.-J. Kim, S.-J. Kim, The effect of post-weld heat treatment affecting corrosion resistance and hydrogen embrittlement of HAZ part in FCAW, Surf. Coatings Technol. 169–170 (2003) 675–678. https://doi.org/10.1016/s0257-8972(03)00060-4.

[6] T. Hemmingsen, H. Hovdan, P. Sanni, N.O. Aagotnes, The influence of electrolyte reduction potential on weld corrosion, Electrochim. Acta. 47 (2002) 3949–3955. https://doi.org/10.1016/S0013-4686(02)00366-3.

[7] G.A. Zhang, Y.F. Cheng, Micro-electrochemical characterization of corrosion of welded X70 pipeline steel in near-neutral pH solution, Corros. Sci. 51 (2009) 1714–1724. https://doi.org/10.1016/j.corsci.2009.04.030.

[8] J. Luo, S. Luo, L. Li, L. Zhang, G. Wu, L. Zhu, Stress corrosion cracking behavior of X90 pipeline steel and its weld joint at different applied potentials in near-neutral

solutions, Nat. Gas Ind. B. 6 (2019) 138–144. https://doi.org/10.1016/j.ngib.2018.08.002.

[9] J.W. Sowards, T. Gnäupel-herold, J.D. Mccolskey, V.F. Pereira, A.J. Ramirez, Characterization of mechanical properties , fatigue-crack propagation , and residual stresses in a microalloyed pipeline-steel friction-stir weld, Mater. Des. 88 (2015) 632–642. https://doi.org/10.1016/j.matdes.2015.09.049.

[10] D.P. Fairchild, A.J. Wasson, A. Kumar, M.L. Macia, T.D. Anderson, Fractographic Investigation of Cleavage Initiation in Steel Friction Stir Welds, in: Trends Weld. Res. 9th Int. Conf., 2012: pp. 193–200.

[11] Z.Y. Liu, X.G. Li, C.W. Du, L. Lu, Y.R. Zhang, Y.F. Cheng, Effect of inclusions on initiation of stress corrosion cracks in X70 pipeline steel in an acidic soil environment, Corros. Sci. 51 (2009) 895–900. https://doi.org/10.1016/j.corsci.2009.01.007.

[12] H. Zhang, D. Wang, P. Xue, L.H. Wu, D.R. Ni, Z.Y. Ma, Microstructural evolution and pitting corrosion behavior of friction stir welded joint of high nitrogen stainless steel, Mater. Des. 110 (2016) 802–810. https://doi.org/10.1016/j.matdes.2016.08.048.

[13] G. Khalaj, M.J. Khalaj, Investigating the corrosion of the Heat-Affected Zones (HAZs) of API-X70 pipeline steels in aerated carbonate solution by electrochemical methods, Int. J. Press. Vessel. Pip. 145 (2016) 1–12. https://doi.org/10.1016/j.ijpvp.2016.06.001.

[14] S. Bordbar, M. Alizadeh, S.H. Hashemi, Effects of microstructure alteration on corrosion behavior of welded joint in API X70 pipeline steel, Mater. Des. 45 (2013) 597–604. https://doi.org/10.1016/j.matdes.2012.09.051.

[15] J.A. Avila, E. Lucon, J.W. Sowards, P.R. Mei, A.J. Ramirez, Assessment of Ductile-to-Brittle Transition Behavior of Localized Microstructural Regions in a Friction-Stir Welded X80 Pipeline Steel with Miniaturized Charpy V-Notch Testing, Metall. Mater. Trans. A. 47 (2016) 2855–2865. https://doi.org/10.1007/s11661-016-3473-z.

[16] J. Avila, J. Rodriguez, P. Roberto, A.J. Ramirez, Microstructure and fracture toughness of multipass friction stir welded joints of API-5L-X80 steel plates, Mater. Sci. Eng. A. 673 (2016) 257–265. https://doi.org/10.1016/j.msea.2016.07.045.

[17] W. Wang, R. Xu, Y. Hao, Q. Wang, L. Yu, Q. Che, J. Cai, K. Wang, Z. Ma, Corrosion fatigue behavior of friction stir processed interstitial free steel, J. Mater. Sci. Technol. 34 (2018) 148–156. https://doi.org/10.1016/j.jmst.2017.11.013.

[18] D.M. Sekban, S.M. Aktarer, G. Purcek, Friction Stir Welding of Low-Carbon Shipbuilding Steel Plates: Microstructure, Mechanical Properties, and Corrosion Behavior, Metall. Mater. Trans. A. 50 (2019) 4127–4140. https://doi.org/10.1007/s11661-019-05324-8.

[19] T.F.C. Hermenegildo, T.F.A. Santos, E.A. Torres, C.R.M. Afonso, A.J. Ramirez,

Microstructural Evolution of HSLA ISO 3183 X80M (API 5L X80) Friction Stir Welded Joints, Met. Mater. Int. 24 (2018) 1120–1132. https://doi.org/10.1007/s12540-018-0111-x.

[20] J.A. Ávila, C.O.F.T. Ruchert, P.R. Mei, R.R. Marinho, M.T.P. Paes, A.J. Ramirez, Fracture toughness assessment at different temperatures and regions within a friction stirred API 5L X80 steel welded plates, Eng. Fract. Mech. 147 (2015) 176–186. https://doi.org/10.1016/j.engfracmech.2015.08.006.

[21] J.A. Avila, R.A.R. Giorjao, J. Rodriguez, E.B. Fonseca, A.J. Ramirez, Modeling of thermal cycles and microstructural analysis of pipeline steels processed by friction stir processing, Int. J. Adv. Manuf. Technol. 98 (2018) 2611–2618. https://doi.org/10.1007/s00170-018-2408-9.

[22] L. Pan, C.T. Kwok, K.H. Lo, Enhancement in hardness and corrosion resistance of AISI 420 martensitic stainless steel via friction stir processing, Surf. Coatings Technol. 357 (2019) 339–347. https://doi.org/10.1016/j.surfcoat.2018.10.023.

[23] American Society for Testing and Materials, ASTM E45-05 Standard Test Methods for Determining the Inclusion Content of Steel, (2007) 19. https://doi.org/10.1520/E0045-05E03.2.

[24] ASTM E3, E3-11 Standard Guide for Preparation of Metallographic Specimens 1, ASTM B. Stand. i (2011) 1–12. https://doi.org/10.1520/E0003-11.2.

[25] ASTM E384, Standard Test Method for Microindentation Hardness of Materials, 2017. https://doi.org/10.1520/E0384-17.

[26] J. Avila, J. Escobar, B. Cunha, W. Magalhães, P. Mei, J. Rodriguez, H. Pinto, A. Ramirez, Physical simulation as a tool to understand friction stir processed X80 pipeline steel plate complex microstructures, J. Mater. Res. Technol. (2018) 1–10. https://doi.org/10.1016/j.jmrt.2018.09.009.

[27] S. Zajac, V. Schwinn, K.H. Tacke, Characterisation and Quantification of Complex Bainitic Microstructures in High and Ultra-High Strength Linepipe Steels, Mater. Sci. Forum. 500–501 (2009) 387–394. https://doi.org/10.4028/www.scientific.net/msf.500-501.387.

[28] G.A. Faria, Exploring metallic materials behavior through in situ crystallographic studies by synchrotron radiation, University of Campinas, 2014.

[29] H. Tristijanto, M.N. Ilman, P. Tri Iswanto, Corrosion Inhibition of Welded of X – 52 Steel Pipelines by Sodium Molybdate in 3.5% NaCl Solution, Egypt. J. Pet. (2020) 1–8. https://doi.org/10.1016/j.ejpe.2020.02.001.

[30] E.E.E. Stansbury, R.A.A. Buchanan, Fundamentals of Electrochemical Corrosion, 2000.

[31] T.F.A. Santos, T.F.C. Hermenegildo, C.R.M. Afonso, R.R. Marinho, M.T.P. Paes, A.J. Ramirez, Fracture toughness of ISO 3183 X80M (API 5L X80) steel friction stir welds, Eng. Fract. Mech. 77 (2010) 2937–2945. https://doi.org/10.1016/j.engfracmech.2010.07.022.

[32] J.A. Avila, F.F. Conde, H.C. Pinto, J. Rodriguez, F.A.F. Grijalba, Microstructural and Residuals Stress Analysis of Friction Stir Welding of X80 Pipeline Steel Plates Using Magnetic Barkhausen Noise, J. Nondestruct. Eval. 38 (2019) 1–9. https://doi.org/10.1007/s10921-019-0625-2.

[33] T.N. Baker, S. Rahimi, B. Wei, K. He, N.A. Mcpherson, Evolution of Microstructure During Double-Sided Friction Stir Welding of Microalloyed Steel, (2019). https://doi.org/10.1007/s11661-019-05184-2.

[34] Y. Wang, G. Cheng, W. Wu, Y. Li, Role of inclusions in the pitting initiation of pipeline steel and the effect of electron irradiation in SEM, Corros. Sci. 130 (2018) 252–260. https://doi.org/10.1016/j.corsci.2017.10.029.

[35] T.Y. Jin, Y.F. Cheng, In situ characterization by localized electrochemical impedance spectroscopy of the electrochemical activity of microscopic inclusions in an X100 steel, Corros. Sci. 53 (2011) 850–853. https://doi.org/10.1016/j.corsci.2010.11.026.

[36] J.M. Quispe-Avilés, D. Hincapie-Ladino, N.A. Falleiros, H.G. de Melo, A Comparative Investigation of the Corrosion Resistance and HIC Suceptibility of API 5L X65 and API 5L X80 Steels, Mater. Res. 22 (2019) 1–13. https://doi.org/10.1590/1980-5373-mr-2018-0191.

[37] L. Sharma, R. Chhibber, Microstructure evolution and electrochemical corrosion behaviour of API X70 linepipe steel in different environments, Int. J. Press. Vessel. Pip. 171 (2019) 51–59. https://doi.org/10.1016/j.ijpvp.2019.01.013.

[38] M. Alizadeh, S. Bordbar, The influence of microstructure on the protective properties of the corrosion product layer generated on the welded API X70 steel in chloride solution, Corros. Sci. 70 (2013) 170–179. https://doi.org/10.1016/j.corsci.2013.01.026.

[39] C.W. Du, X.G. Li, P. Liang, Z.Y. Liu, G.F. Jia, Y.F. Cheng, Effects of Microstructure on Corrosion of X70 Pipe Steel in an Alkaline Soil, 18 (2009) 216–220. https://doi.org/10.1007/s11665-008-9280-y.

[40] N. Ochoa, C. Vega, N. Pébère, J. Lacaze, J.L. Brito, CO2 corrosion resistance of carbon steel in relation with microstructure changes, Mater. Chem. Phys. 156 (2015) 198–205. https://doi.org/10.1016/j.matchemphys.2015.02.047.

[41] J.R. da Cruz, R. Bertazzoli, Characterization of Corrosion Within Friction Stir Weld Zones of an API X-70 Steel Using a Novel Microcell Setup, J. Mater. Eng. Perform. 29 (2020) 98–108. https://doi.org/10.1007/s11665-019-04531-z.

[42] A. Di Schino, J.M. Kenny, Effects of the grain size on the corrosion behavior of refined AISI 304 austenitic stainless steels, J. Mater. Sci. Lett. 21 (2002) 1631–1634. https://doi.org/10.1023/A:1020338103964.

[43] K.M. Deen, R. Ahmad, I.H. Khan, Z. Farahat, Microstructural study and electrochemical behavior of low alloy steel weldment, Mater. Des. 31 (2010) 3051–3055. https://doi.org/10.1016/j.matdes.2010.01.025.

[44] W. Liu, H. Pan, L. Li, H. Lv, Z. Wu, F. Cao, J. Zhu, Corrosion behavior of the high strength low alloy steel joined by vertical electro-gas welding and submerged arc welding methods, J. Manuf. Process. 25 (2017) 418–425. https://doi.org/10.1016/j.jmapro.2016.12.011.

.